Magnetic, resonance, and optical properties of $Cu_3Sm(SeO_3)_2O_2Cl$: A rare-earth francisite compound

K. V. Zakharov,[1] E. A. Zvereva,[1] M. M. Markina,[1] M. I. Stratan,[1] E. S. Kuznetsova,[1] S. F. Dunaev,[1] P. S. Berdonosov,[1] V. A. Dolgikh,[1] A. V. Olenev,[1,2] S. A. Klimin,[3] L. S. Mazaev,[3,4] M. A. Kashchenko,[3,4] Md. A. Ahmed,[5] A. Banerjee,[5,6] S. Bandyopadhyay,[5,6] A. Iqbal,[7] B. Rahaman,[7] T. Saha-Dasgupta,[8,*] and A. N. Vasiliev[1,9,10,†]

[1]*M.V. Lomonosov Moscow State University, 119991 Moscow, Russia*
[2]*Sine Theta Ltd., 119992 Moscow, Russia*
[3]*Institute of Spectroscopy, RAS, Moscow, 142190 Troitsk, Russia*
[4]*Moscow Institute of Physics and Technology, 141707 Dolgoprudnyi, Russia*
[5]*University of Calcutta, 700009 Kolkata, India*
[6]*Centre for Research in Nanoscience and Nanotechnology, University of Calcutta, Salt Lake, 700098 Kolkata, India*
[7]*Aliah University, 700156 Kolkata, India*
[8]*S.N. Bose National Centre for Basic Sciences, 700098 Kolkata, India*
[9]*Ural Federal University, 620002 Ekaterinburg, Russia*
[10]*National University of Science and Technology "MISiS," 119049 Moscow, Russia*

(Received 3 March 2016; revised manuscript received 7 June 2016; published 1 August 2016)

In this combined experimental and theoretical paper, we study the properties of $Cu_3Sm(SeO_3)_2O_2Cl$ belonging to the francisite family of compounds, which are novel frustrated layered compounds. $Cu_3Sm(SeO_3)_2O_2Cl$ is synthesized through a solid state reaction. Characterizations through measurements of magnetization, specific heat, X-band electron spin resonance, and rare-earth optical spectroscopy, establish that the compound orders antiferromagnetically at $T_N = 35$ K and undergoes a spin-reorientation phase transition at $T_C = 8.5$ K due to the interplay of anisotropies in transition metal and rare-earth subsystems. The ground state Kramers doublet of Sm is found to split only at $T < T_C$ when the exchange field is aligned along the nonzero component of its g factor. Prior to full saturation with $M_s \leqslant 3\,\mu_B$/f.u., which is reached under application of moderate magnetic field, the magnetization is found to exhibit complicated hysteresis behavior related to field-induced metamagnetic phase transitions. The first principles calculations reveal the hierarchy of exchange interaction parameters in the kagome-type magnetic subsystem of $Cu_3Sm(SeO_3)_2O_2Cl$.

DOI: 10.1103/PhysRevB.94.054401

I. INTRODUCTION

Geometrically frustrated layered compounds have generated tremendous research interest in recent time from both scientific and technological viewpoints. Due to the presence of competing interactions, the evolved magnetic properties may exhibit highly unusual features. For example, in the case of a strong ferromagnetic intralayer exchange and a weak antiferromagnetic interlayer coupling, the magnetic ground state of antiferromagnetically arranged ferromagnetic layers can be easily broken by external magnetic fields, which enable simple switching between zero and maximum magnetization. The apparent metamagnetic response due to this, which is an abrupt change of the bulk magnetization, thus becomes useful in high-density magnetic storage and spintronics devices. Further, the ability to synthesize geometrically frustrated magnetic compounds in a layered structure allows for a study of a quasi-two-dimensional model of a three-dimensional system.

In the above context, the mineral francisite $Cu_3Bi(SeO_3)_2O_2Cl$ [1,2] and its synthetic analogues $Cu_3Bi(SeO_3)_2O_2X$ (X = Cl, Br, I) [3–5], $Cu_3Bi(TeO_3)_3O_2Cl$ [6], and $Cu_3Y(SeO_3)_2O_2Cl$ [7] are recently in the focus of intensive experimental and theoretical study. At present, the francisites $Cu_3Ln(ChO_3)_2O_2X$ (Ln = Bi, Y, rare earth; Ch = Se, Te; X = Cl, Br, I) constitute vast and largely uninvestigated family of compounds. The attractive feature of francisite's crystal structure is the buckled kagome motif in the arrangement of transition metal ions. This motif suppresses or may even prevent the formation of long range ordered magnetic structures for competing antiferromagnetic interactions [8]. The pristine mineral, $Cu_3Bi(SeO_3)_2O_2Cl$, experiences structural transformation following very anisotropic thermal expansion at elevated temperatures [2], while no signatures of such transformation are found for any other investigated member of this family. Two francisites, $Cu_3Bi(SeO_3)_2O_2Br$ [5] and $Cu_3Y(SeO_3)_2O_2Cl$ [7], studied in neutron scattering measurements possess noncollinear six-sublattices magnetic network based on a buckled kagome crystal structure. In the case of a dominant ferromagnetic interaction, however, the kagome type lattice may support canted configuration of magnetic moments. It was shown that the competing exchange interactions along with Dzyaloshinsky-Moriya interactions are responsible for the highly unusual noncollinear six-sublattices magnetic ground state in francisites [9]. The overall antiferromagnetic structure is rather fragile, being subject to metamagnetic phase transition prior to attaining the full saturation in moderate magnetic field.

The crystal structure of francisite allows the substitution of generic bismuth by virtually all rare-earth (RE) ions in a row from La to Lu, excluding Ce [10]. The presence of RE ions in

*Corrresponding author: t.sahadasgupta@gmail.com
†Corrresponding author: vasil@lt.phys.msu.ru

the francisite's structure adds a new dimension to the physics of these systems. It not only brings in the complications of an additional magnetic sublattice due to the presence of a RE cation, but the interplay of magnetic anisotropies also becomes important. The orbital motion of the electrons in REs is not quenched, so both spin and orbital components contribute to the overall magnetic moment. The RE magnetic subsystem may influence the magnetic subsystem of transition metal resulting in complex transformations of the overall magnetic structure. The preliminary studies of the RE francisites have revealed amazing variety in magnetic response within this family of compounds. To understand the complex behavior of these RE francisites, we start our investigation with $Cu_3Sm(SeO_3)_2O_2Cl$. The measurements of magnetization, specific heat, and electron spin resonance (ESR) in this compound were supplemented by a spectroscopic study of *f-f* transitions in a Sm^{3+} Kramers ion. The qualitative similarity of the response to the external magnetic field observed in thermodynamic measurements of $Cu_3Sm(SeO_3)_2O_2Cl$ sample in comparison to $Cu_3Bi(SeO_3)_2O_2Br$ [5] and $Cu_3Y(SeO_3)_2O_2Cl$ [7] samples indicates that the canted magnetic structure is a general feature of all francisite compounds. The first principles calculations of $Cu_3Sm(SeO_3)_2O_2Cl$ provides the estimates of the exchange interaction parameters, and comparison is made with that obtained for earlier investigated francisites. The comparison is expected to provide us with the understanding of the role of magnetism of RE ions, which may be useful in understanding the RE ion based francisite compounds in general.

II. SYNTHESIS AND CRYSTAL STRUCTURE

$Cu_3Sm(SeO_3)_2O_2Cl$ was prepared from a stoichiometric mixture of high purity Sm_2O_3, CuO, $CuCl_2$, and SeO_2. The selenium dioxide was obtained from selenous acid (98%), which was dehydrated under dynamic vacuum at a moderate temperature and then sublimed in a flowing mixture of dry air and NO_2 prepared by thermal decomposition of $Pb(NO_3)_2$. All preparatory procedures with SeO_2 were carried out in a dry box purged with argon. The stoichiometric reactant mixture (about 1 g in total) was thoroughly ground in an agate mortar and transferred into quartz tube that was sealed under vacuum and placed into an annealing furnace with controlled heating. The mixture was heated to 300 °C over 12 h and kept at this temperature for 24 h. Then the temperature was raised to 575 °C over 12 h and maintained at this temperature for 72 h. A green powder sample was produced.

Preliminary characterization by powder x-ray diffraction collected on a Stoe Stadi-P diffractometer equipped with a germanium monochromator ($CuK\alpha_1$ radiation) in the 2θ range of $10°-115°$ with a step of $0.01°$ confirmed phase purity according to the previously suggested structural model for $Cu_3Sm(SeO_3)_2O_2Cl$ [10]. Final data collection for the refinement of crystal structure of the sample synthesized was done on a PANalytical Empyrean diffractometer [Cu x-ray tube, Ni-filter ($CuK\alpha_1$, $CuK\alpha_2$), Bragg-Brentano geometry, 2θ range $10°-120°$ with a step of $0.017°$] equipped with an X'celerator linear detector. The resulting x-ray diffraction patterns were processed by a JANA2006 program [11]. As the initial model, the structural data for $Cu_3Bi(SeO_3)_2O_2Cl$ was used [3]. The x-ray diffraction experiment details and crystal data are summarized in Table I, the atomic coordinates and thermal parameters are given in Table II, and selected interatomic distances are in Table III. The final Rietveld refinement profiles are shown in Fig. 1.

TABLE I. Crystal data and x-ray diffraction details for $Cu_3Sm(SeO_3)_2O_2Cl$.

System	Orthorombic
Space group	*Pmmn*
Instrument	PANalytical Empyrean
Unit cell parameters	
a, Å	6.34616(4)
b, Å	9.56090(7)
c, Å	7.04377(5)
Z	2
2θ range, °	10–120
Temperature, K	293
The number of refined parameters	34
R_p	0.0251
wR_p	0.0332
wR exp	0.0263
Goodness of Fit	1.26

$Cu_3Sm(SeO_3)_2O_2Cl$ has an orthorhombic primitive cell with two formula units per unit cell. There are two inequivalent positions for copper ions, Cu1 and Cu2, standing at the center of a distorted square constructed by four O-ions. The Cu-O bond lengths range from 1.899 to 1.997 Å, with an average value of 1.954 Å. The crystal structure of $Cu_3Sm(SeO_3)_2O_2Cl$ is shown in Fig. 2. The distorted $Cu1O_4$ squares share a common corner with each other and form chains along a direction. Chains are connected in the b direction by the distorted $Cu2O_4$ squares and form layers in the ab plane. Inside the layer, Cu1 and Cu2 ions unite into buckled kagome network. The plane of the distorted $Cu2O_4$ square is perpendicular to the ab plane. The layers are connected by Sm atoms along the c direction and form a three-dimensional network; $Cu1O_4$ and $Cu2O_4$ squares also share a common corner.

The special feature of the francisite's crystal structure has to be mentioned. It belongs to inclusion compounds that bear a positive charge on the host. The guest halide ions reside in the tunnels running along the [001] axis, not covalently bonded

TABLE II. Atomic coordinates and isotropic thermal parameters in $Cu_3Sm(SeO_3)_2O_2Cl$.

Atom	Position	x	y	z	U_{iso}, Å^2
Sm1	2*a*	1/4	1/4	0.2664(2)	0.0136(6)
Cu1	4*c*	0	0	0	0.0387(9)
Cu2	2*a*	1/4	1/4	0.7960(5)	0.0263(12)
Se1	4*e*	1/4	0.5568(2)	0.5967(3)	0.0208(7)
Cl1	2*b*	1/4	3/4	0.1449(9)	0.058(3)
O1	4*e*	1/4	0.1148(10)	1.0068(14)	0.036(4)
O2	8*g*	0.033(1)	0.5865(6)	0.7422(11)	0.038(3)
O3	4*e*	1/4	0.1252(8)	0.5741(13)	0.005(3)

TABLE III. Interatomic distances (d) in the structure of $Cu_3Sm(SeO_3)_2O_2Cl$.

Bond		d, Å
Sm1–O1	×2	2.308(8)
Sm1–O2	×4	2.457(5)
Sm1–O3	×2	2.518(8)
Cu1–Cl1	×2	3.048(2)
Cu1–O1	×2	1.904(4)
Cu1–O2	×2	1.998(6)
Cu2–Cl1	×2	3.2003(7)
Cu2–O1	×2	1.968(8)
Cu2–O3	×2	1.953(8)
Se1–O2	×2	1.688(6)
Se1–O3	×1	1.724(7)

to any framework metal ions. The practical significance of this fact, i.e., the enhanced mobility of anions, is hampered, however, by the fact that the chalcogens retain their lone pair of electrons pointed into the channels. This circumstance effectively blocks the anion mobility [12].

III. THERMODYNAMICS

The magnetization and dc-susceptibility data were taken on a Quantum Design Magnetic Property Measurement System MPMS-7T over the temperature range 2–400 K in applied field strengths up to 7 T, while the magnetization data up to 9 T were taken on a Quantum Design Physical Property Measurement System PPMS-9T. The temperature dependences of magnetic susceptibility χ in $Cu_3Sm(SeO_3)_2O_2Cl$ taken in both zero field cooled (ZFC) and field cooled (FC) regimes at $B = 0.02$ T in the range 2–75 K are shown in Fig. 3. At elevated temperatures, these dependences coincide and can be approximated by the sum of temperature independent term χ_0 and contributions of RE and transition metal subsystems

$$\chi = \chi_0 + N_A \mu_B^2 g_J^2 \frac{J(J+1)}{3k_B T} + \frac{C}{T-\Theta}. \qquad (1)$$

The χ_0 itself consists of diamagnetic response of every ion equal to the sum of individual Pascal's constants [13]

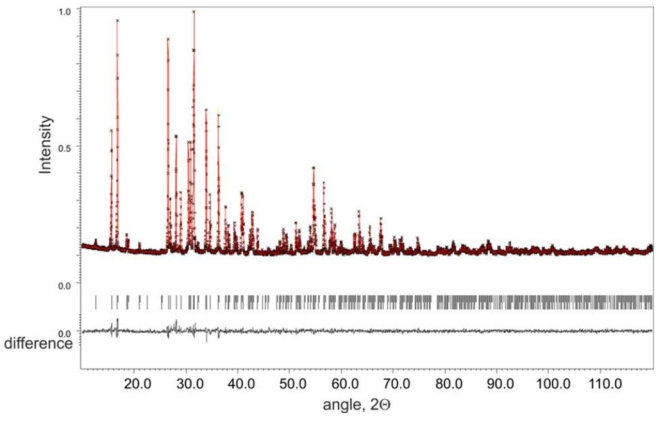

FIG. 1. The Rietveld refinement plot for $Cu_3Sm(SeO_3)_2O_2Cl$.

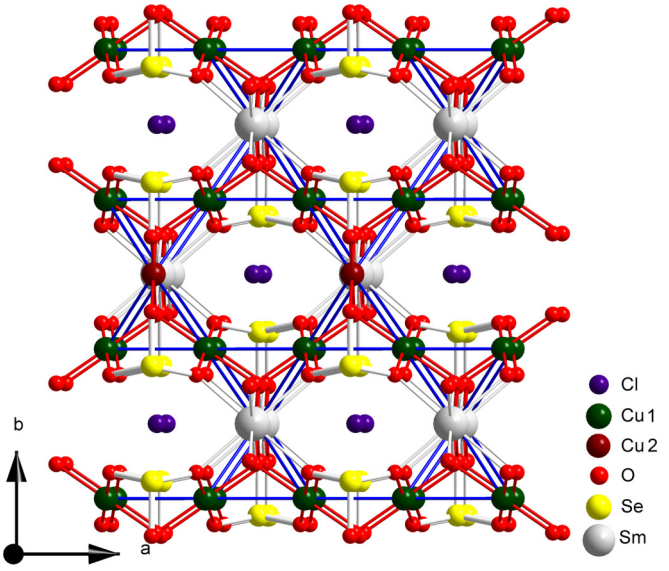

FIG. 2. The crystal structure of $Cu_3Sm(SeO_3)_2O_2Cl$. The solid lines connecting the Cu ions underline the kagome motif in the structure.

plus van Vleck terms of Cu^{2+} [14] and Sm^{3+} [15] ions. In total, the positive value of $\chi_0 = 7.6 \times 10^{-4}$ emu mol^{-1} is mostly defined by van Vleck magnetism of Sm^{3+} ions. The temperature dependent contribution of the RE subsystem can be modeled by the Curie law assuming virtually noninteracting Sm^{3+} centers with $g_J = 2/7$ and $J = 5/2$. This term is important at low temperatures but is rather small at high temperatures. In the upper temperature range 200–320 K, the paramagnetic response in $Cu_3Sm(SeO_3)_2O_2Cl$ is defined by the Curie-Weiss type contribution of Cu^{2+} ions with the Curie constant $C = 1.6$ emu mol^{-1} K and Weiss temperature $\Theta = 52$ K. The positive sign of Weiss temperature indicates the predominance of ferromagnetic exchange interactions at

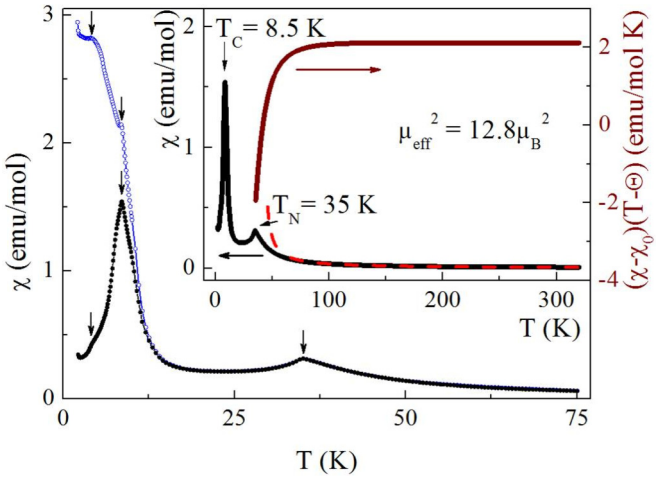

FIG. 3. The temperature dependences of magnetic susceptibility in $Cu_3Sm(SeO_3)_2O_2Cl$ in ZFC (squares) and FC (circles) regimes taken at $B = 0.02$ T. Inset: The ZFC curve in the range 2–320 K and its fit (dash) in accordance with Eq. (1). Also shown is the temperature dependence of Curie constant $C = (\chi - \chi_0)(T - \Theta)$.

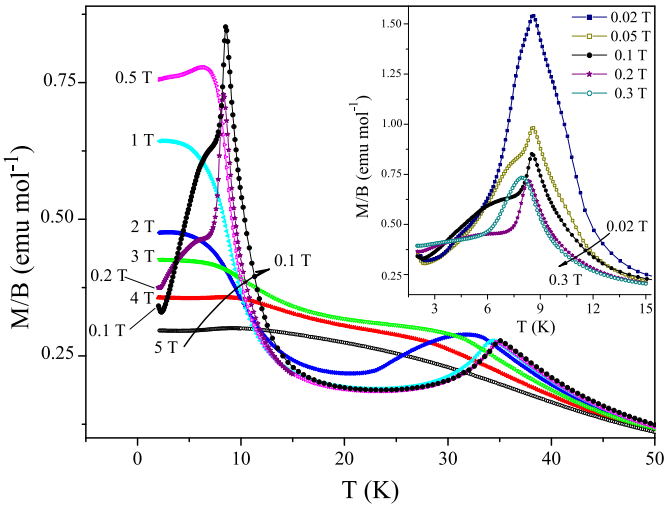

FIG. 4. The temperature dependences of reduced magnetization M/B in $Cu_3Sm(SeO_3)_2O_2Cl$ taken at various magnetic fields in ZFC regime. Inset: M/B vs T dependences at low magnetic fields in vicinity of T_C.

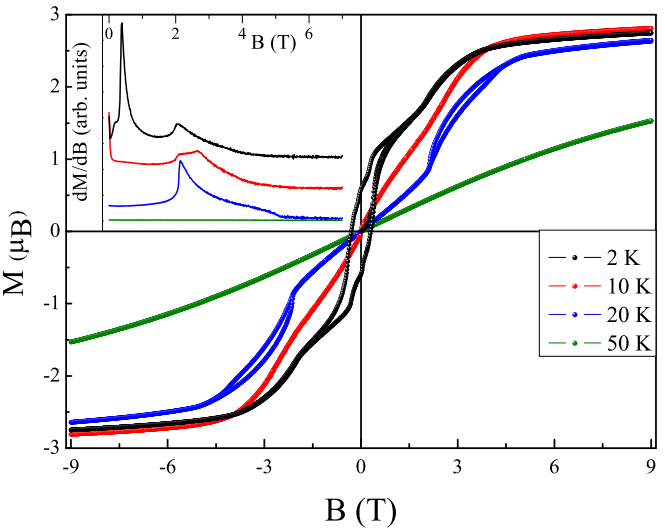

FIG. 5. The field dependences of $Cu_3Sm(SeO_3)_2O_2Cl$ magnetization at selected temperatures. Inset: Field dependence of magnetization derivatives dM/dB.

elevated temperatures, while the Curie constant C yields an effective magnetic moment squared $\mu_{\text{eff}}^2 = 12.8\,\mu_B^2$ per formula unit with three Cu^{2+} ions with spin $S = 1/2$. The inset to Fig. 3 shows ZFC magnetic susceptibility in the whole temperature range and the temperature dependence of Curie constant $C = (\chi - \chi_0)(T - \Theta)$, which indicates the strengthening of antiferromagnetic exchange interactions upon cooling.

At $T_N = 35$ K, both ZFC and FC curves reach a sharp peak, indicating formation of the long range magnetic order. Below T_N, these dependences deviate from each other, as clearly seen at low temperatures. At $T_C = 8.5$ K, the ZFC curve exhibits another sharp peak, while the FC curve experiences the kink. Below T_C, the broad Schottky-type anomaly is seen in both ZFC and FC curves, while the lowest temperatures reveal the Curie type upturn. The anomaly at T_N can be attributed to the ordering of transition metal subsystem similar to long-range ordering in Bi and Y francisites [3–5,7]. The origin of the sharp anomaly at T_C is assumingly the spin-reorientation transition due to the *f-d* interaction in $Cu_3Sm(SeO_3)_2O_2Cl$. The Schottky-type anomaly could be related to the splitting of Sm^{3+} ion levels, while the low temperature upturn is due to defects/impurities contribution.

The temperature dependences of reduced magnetization M/B in $Cu_3Sm(SeO_3)_2O_2Cl$ taken at various magnetic fields up to 5 T are shown in Fig. 4. The sharp features evident in $\chi(T)$ curve taken at low magnetic field smears upon application of an external magnetic field and shift to lower temperatures. The magnetic response of the title compound in vicinities of T_N and T_C differs, however. The main difference is the fast suppression of the anomaly at T_C, as shown in the inset of Fig. 4. Besides, the Schottky-type anomaly and low temperature upturn of magnetization disappear in moderate magnetic fields.

The field-induced transformations of the magnetic subsystem in $Cu_3Sm(SeO_3)_2O_2Cl$ lead to very complicated field dependences of magnetization $M(B)$, as shown in Fig. 5. Above T_N, the magnetization curve is linear at low magnetic field and tends to saturation at high magnetic field, as expected for paramagnetic state. In the $T_C < T < T_N$ range, the loop is seen on the $M(B)$ curve, which evidences the field-induced first order phase transition in the transition metal subsystem. The overall behavior of magnetization in this temperature range is consistent with succession of metamagnetic and spin-flip transitions, as shown in the inset of Fig. 5. Approaching T_C from above the loop in high magnetic fields closes, but another loop opens below T_C. This loop demonstrates several inflections: At 2 K it has residual magnetization $0.625\,\mu_B$ and coercive field 0.3 T. Assumingly the complicated shape of the loop at low temperatures results from the competition of RE and transition metal single-ion anisotropies. Besides, the anisotropic response of $Cu_3Sm(SeO_3)_2O_2Cl$ is averaged over various crystal axes in the powder sample. Note, that the marked difference in response to the magnetic field applied along different crystal axes was seen in the single crystal of $Cu_3Bi(SeO_3)_2O_2Cl$ [4].

At low temperatures, the magnetization in $Cu_3Sm(SeO_3)_2O_2Cl$ varies nonmonotonously and reaches saturation $M_s \sim (2.7 \pm 0.1)\,\mu_B$ in moderate magnetic field. The variations are due tentatively to the influence of RE anisotropy. The saturation magnetization value M_s is constituted by contributions of RE $M_s^{\text{Sm}} = g_J J \mu_B \sim 0.7\,\mu_B$ and transition metal $M_s^{\text{Cu}} = 3gS\mu_B \sim 3.3\,\mu_B$ subsystems. The value of saturation magnetization indicates that the RE and transition metal moments couple antiferromagnetically, i.e., $M_s \sim M_s^{\text{Cu}} - M_s^{\text{Sm}}$. Besides, the magnetic moments residing on Cu^{2+} ions can be reduced, as estimated in Ref. [9].

The specific heat C_p was measured on a pressed pellet sample of few mg of $Cu_3Sm(SeO_3)_2O_2Cl$ using relevant option of Quantum Design PPMS-9T by relaxation method in the temperature range 2–250 K in magnetic field up to 9 T. No anomalies were seen in $C_p(T)$ curve above T_N, which excludes the structural phase transition seen in $Cu_3Bi(SeO_3)_2O_2Cl$ below room temperature [4]. The temperature dependences of specific heat in $Cu_3Sm(SeO_3)_2O_2Cl$ in the range 2–50 K

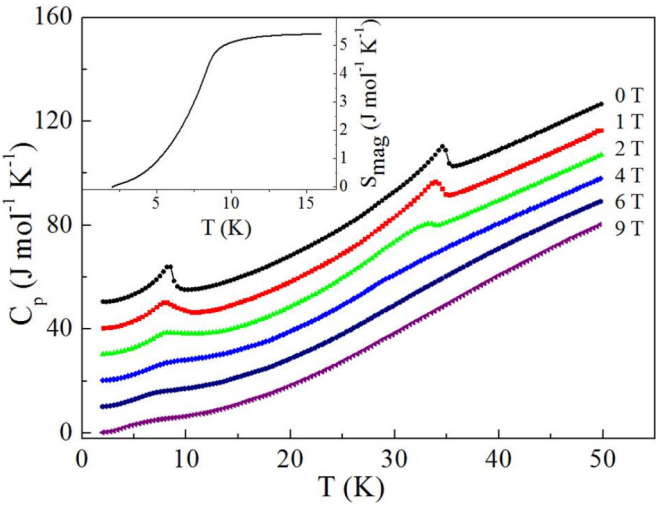

FIG. 6. The temperature dependences of $Cu_3Sm(SeO_3)_2O_2Cl$ specific heat in selected magnetic fields. Inset: Temperature dependence of magnetic entropy S_{mag}.

taken at various magnetic fields are shown in Fig. 6. The $C_p(T)$ curves demonstrate two smeared λ-type anomalies at T_N and T_C, but no Schottky-type anomaly is seen below T_C. The λ-type anomalies of comparable magnitudes evidence two successive second order phase transitions in transition metal subsystem. An external magnetic field rapidly suppresses both phase transitions, but that at T_C is somewhat more robust. To estimate the entropy released at T_C, the reference specific heat data obtained on $Cu_3Y(SeO_3)_2O_2Cl$ were used [5]. The subtraction of scaled Y francisite data from that in Sm francisite in the range 2–20 K allows estimating the magnetic entropy released at T_C as $\Delta S_{mag} = 5\,J\,mol^{-1}\,K^{-1}$ to be compared with total magnetic entropy of transition metal subsystem $3R\ln 2 = 17.3\,J\,mol^{-1}\,K^{-1}$.

IV. ELECTRON SPIN RESONANCE

The ESR studies were carried out using an X-band ESR spectrometer CMS 8400 (Adani) equipped with a low temperature mount, operating in the range $T = 5-300$ K. The effective g factor has been calculated with respect to a BDPA reference sample. The temperature evolution of the powder ESR spectra in $Cu_3Sm(SeO_3)_2O_2Cl$ is shown in Fig. 7. The ESR spectrum in paramagnetic phase represents a broad absorption line that is a superposition of two main components: wide L^w and narrow L^n, as denoted in Fig. 7(b). Both resonance modes are characterized by a comparable resonance field. The line L^w narrows markedly with decreasing temperature, and both modes increase in amplitude [Fig. 7(a)] so the presence of these main features is most obvious in the temperature range 40–70 K [Fig. 7(b)]. In the vicinity of Néel temperature, the broad background line L^w disappears, while the line L^n shows anisotropic character and remains detectable down to second characteristic temperature T_C [Fig. 7(c)]. Below this point, the degradation of the paramagnetic resonance signal eventually occurs, and this signal fading is usually associated with opening of the gap for resonance excitations in a magnetically ordered state.

Remarkably, the overall behavior of the ESR absorption is quite similar to recently reported data for the isostructural compound $Cu_3Y(SeO_3)_2O_2Cl$ [7]. Hence, it seems reasonable to use the interpretation and analysis procedure suggested for the yttrium analogue. Thus, two resonance modes might be assigned to two different Cu^{2+} sites in the crystal structure of

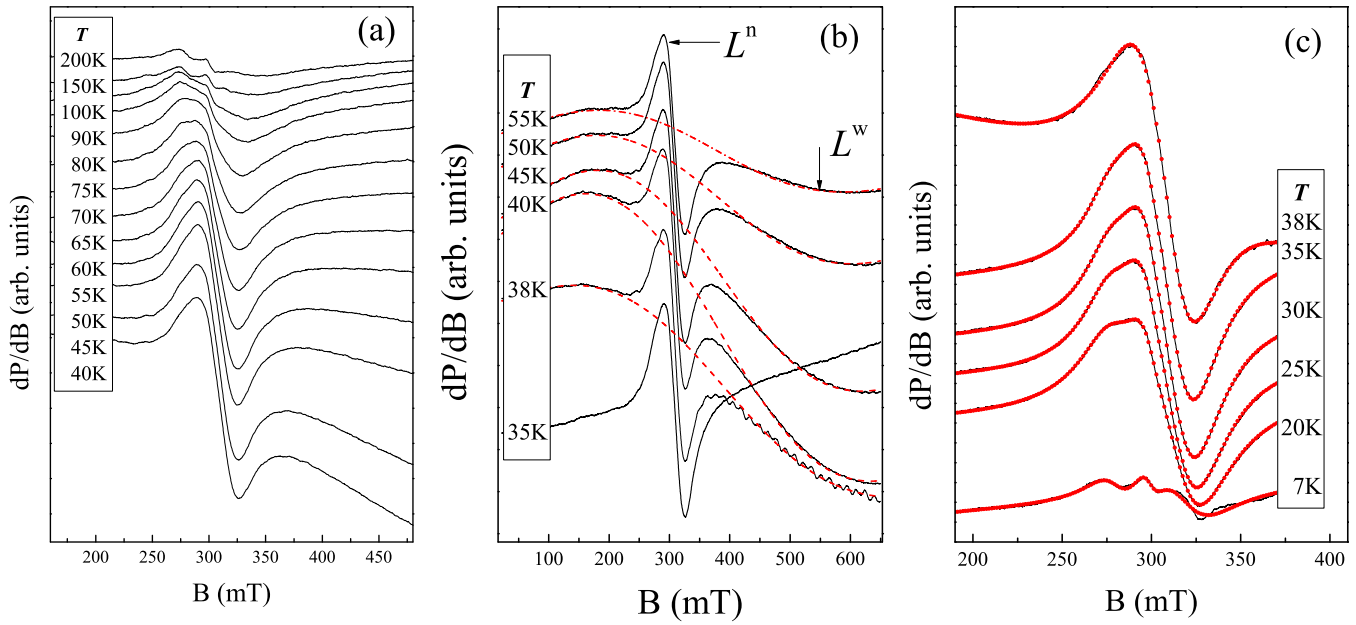

FIG. 7. The temperature evolution of ESR spectra of $Cu_3Sm(SeO_3)_2O_2Cl$ in different temperature ranges: (a) the high temperature range where the superposition of two modes was observed; (b) the temperature range in the vicinity of Néel temperature (55–35 K) highlighting the disappearance of the L^w mode below T_N, with dashed red lines representing fitting of the L^w resonance mode by Lorentzian profile; (c) the low temperature range showing the behavior of L^n mode below T_N, with solid red lines representing fitting of the L^n resonance mode by sum of three Lorentzians, as described in the text. The two resonance modes revealed are denoted by the arrows in the middle panel (b).

$Cu_3Sm(SeO_3)_2O_2Cl$, as shown in Fig. 2. The internal magnetic fields effectively suppress the paramagnetic ESR signal from the Cu2 site at temperatures below T_N, while the signal from the Cu1 remains present even in the low temperature phase $T < T_N$, similar to the case $Cu_3Y(SeO_3)_2O_2Cl$ [7] and mixed dimensionality system CuP_2O_6 [16].

A precise quantitative analysis of the ESR line L^w is rather complicated due to its extremely large linewidth over almost the whole temperature range studied. Nevertheless, in order to get some quantitative estimations for the L^w mode, we have fitted the spectra in the temperature range 40–80 K, in accordance with Lorentzian profile [17], taking into account two circular components of the exciting linearly polarized microwave field on both sides of $B = 0$,

$$\frac{dP}{dB} \propto \frac{d}{dB}\left[\frac{\Delta B}{\Delta B^2 + (B - B_r)^2} + \frac{\Delta B}{\Delta B^2 + (B + B_r)^2}\right], \quad (2)$$

where P is the power absorbed in the ESR experiment, B is the applied magnetic field, B_r is the resonance field, and ΔB is the linewidth. Note that during this analysis, we have neglected the middle part of the spectrum related to another component L^n. The fitted curves are shown by dashed lines in Fig. 7(b). The effective g factor for line L^w was found to be about $g = 2.1 \pm 0.1$, while its linewidth exceeds 400 mT at 40 K and markedly increases with increasing temperature.

To evaluate the main ESR parameters of the anisotropic line L^n, the experimental spectra have been fitted by a sum of three components corresponding to the principal values of the g tensor by analogy with fitting procedure used for $Cu_3Y(SeO_3)_2O_2Cl$ [7]. The temperature dependences of the effective g factor and linewidth derived from this fitting are shown in the upper and middle panels of Fig. 8. Both the g factor and the linewidth vary weakly over the wide temperature range studied. The average values of the anisotropic g tensor are $g_1 = 2.35(4)$, $g_2 = 2.20(5)$, and $g_3 = 2.06(7)$, resulting in $g = 2.20 \pm 0.02$, which is comparable to both the g values reported for the isostructural compounds $Cu_3Bi(SeO_3)_2O_2Br$ [$g = 2.04(8)$] [18], $Cu_3Bi(SeO_3)_2O_2Cl$ ($g = 2.16$) [4], and $Cu_3Y(SeO_3)_2O_2Cl$ ($g = 2.115 \pm 0.005$) [7]. A slight difference in behavior of ΔB_1, ΔB_2, and ΔB_3 indicates that the correlations in $Cu_3Sm(SeO_3)_2O_2Cl$ are evolving in an anisotropic manner. The temperature-dependent anisotropies of interplaying RE and copper subsystems might be responsible for variation of ratio between spin-spin and spin-lattice relaxation rates. As can be seen in Fig. 8, all ESR parameters of L^n mode demonstrate a clear anomaly at T_N, and the integral ESR intensity is in reasonable agreement with static magnetic susceptibility (cf. lower panel in Fig. 8). Both the resonance field and the linewidth pass through a maximum in the vicinity of the Néel temperature. The second characteristic temperature T_C is also detectable both from dynamic and static data.

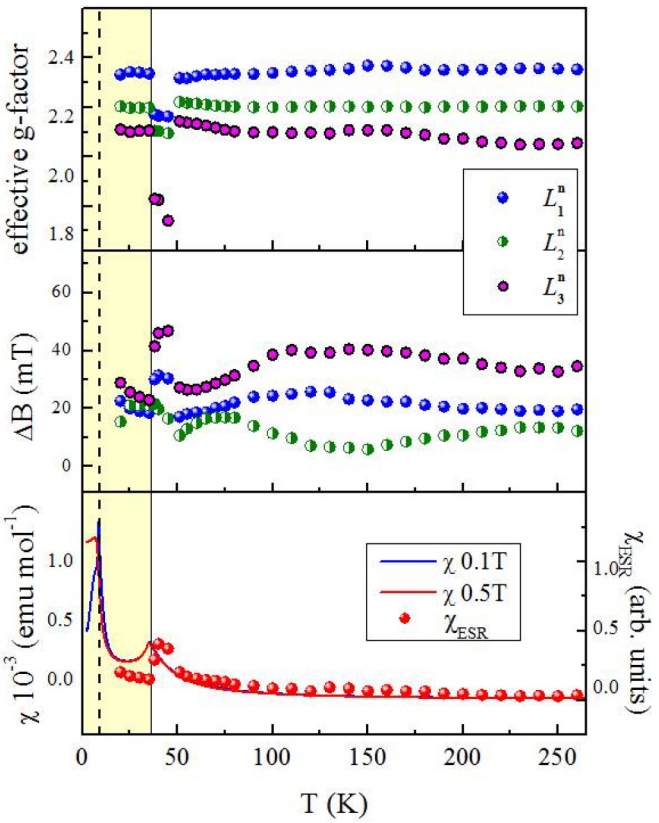

FIG. 8. The temperature dependence of principal values of g tensor (upper panel), the ESR linewidth for three resolved components (middle panel), and the integral ESR intensity for L^n mode (red filled circles) in comparison with static magnetic susceptibility data (lower panel).

V. OPTICAL SPECTROSCOPY

For optical spectroscopy measurements, 15 mg of $Cu_3Sm(SeO_3)_2O_2Cl$ was thoroughly ground in agate mortar, mixed with an optical-grade KBr (250 mg), and pressed into a pellet, which was put into the optical close-cycled cryostat CRYOMECH PT-403. The transmission spectroscopy experiment was done with the aid of Bruker IFS125HR Fourier-transform spectrometer in a wide spectral 2000−10 000 cm^{-1} and temperature 4–300 K ranges.

The spectroscopic information was obtained on more than 31 crystal field levels for the f-f transitions in Sm^{3+} from the ground $^6H_{5/2}$ to 10 excited $^6H_{9/2}$-$^6H_{15/2}$, $^6F_{1/2}$-$^6F_{11/2}$ multiplets. Two spectral lines were selected to demonstrate their typical behavior at low temperatures. These are shown in Fig. 9 together with the color intensity maps, where different colors corresponding to certain intensities are used to depict spectral changes in wave number–temperature coordinate plane. Two peculiarities are present at temperatures 35 and 8.5 K. The line at 2586 cm^{-1} (L1) demonstrates drastic narrowing at the temperature 35 K. Such a behavior is typical for the most of spectral lines. The line at 6570 cm^{-1} (L2) splits at this temperature. The splitting of Sm^{3+} Kramers doublet indicates unambiguously the appearance of the magnetic field, as the only perturbation that can split Kramers doublet is a magnetic field [19]. In the case of $Cu_3Sm(SeO_3)O_2Cl$, it is an effective magnetic field B_{eff}, appearing in a magnetically ordered state. As most of the other spectral lines do not experience splitting at the temperature $T_N = 35$ K, we concluded that the ground Kramers doublet does not split at this temperature. The excited Kramers doublet splits for the optical transition

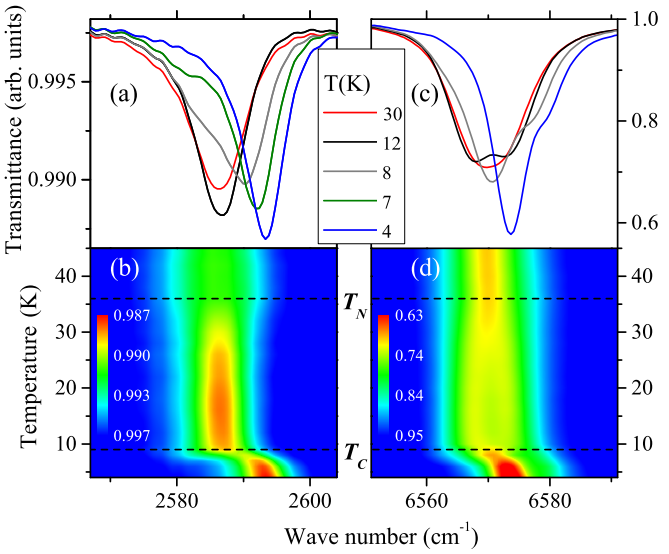

FIG. 9. Two spectral lines due to the Sm^{3+} absorption from (a), (b) $^6H_{15/2}$ -$^6H_{9/2}$ and (c), (d) $^6H_{15/2}$ -$^6H_{3/2}$ transitions. (a), (c) Spectral lines at several temperatures. (b), (d) Intensity maps in the temperature-wave number coordinates.

L2. The scheme shown in Fig. 10(a) (the temperature range $T_C < T < T_N$) illustrates such a behavior.

Another and more pronounced peculiarity in the temperature behavior of crystal field levels of Sm^{3+} is found at $T_C = 8.5$ K. At this temperature, all the spectral lines experience a pronounced shift to higher energies. Careful inspection shows that at this temperature not a simple shift but the splitting of spectral lines occurs. The pronounced shoulder on the high-energy part of the split spectral line L1 at 8 K and the weak separate peak at 7 K confirm this fact. An abrupt decrease in intensity of the high-energy split component is typical for the splitting of the ground Kramers doublet. As this splitting occurs at low enough temperature and it reaches more than 10 cm^{-1} within 1–2 K, the population of the upper component of the split ground Kramers doublet rapidly becomes close to zero, the same happens with the intensity of the optical transitions starting from this level.

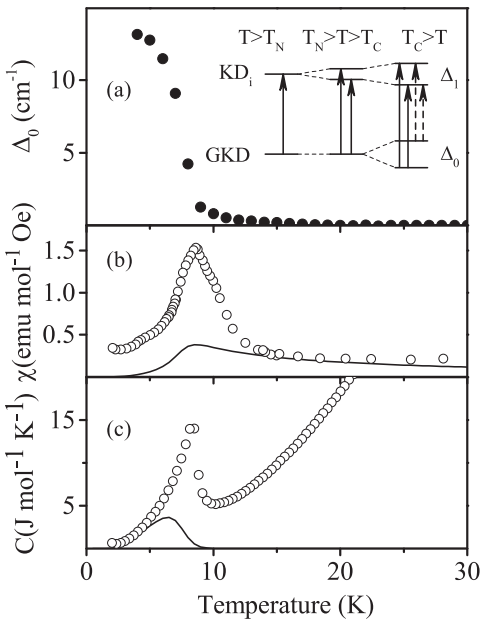

FIG. 10. (a) The splitting Δ_0 as a function of temperature. Inset: A scheme of possible splitting of ground Kramers doublets (GKDs) and excited Kramers doublets (KDs) in Sm^{3+} ion in different magnetic phases; (b) and (c) calculated contribution of samarium (lines) and experimental data (circles) on (b) magnetic susceptibility and (c) heat capacity.

At 4 K, the spectral line L2 (as well as several other lines) consists of two components; the distance between them being equal to the splitting Δ_1 of excited Kramers doublet of corresponding transition. The analysis of temperature behavior for all the lines registered in the experiment allowed us to restore the splitting of the ground Kramers doublet Δ_0 as a function of temperature, as shown in Fig. 10(b). It is equal to zero at temperatures higher that T_C, and then it grows rapidly and reaches the value of 14 cm^{-1} at the lowest temperatures. Such a behavior of $\Delta_0(T)$ is connected with the competition of magnetic anisotropies of two main magnetic subsystems, namely, transition metal and RE ones. The anisotropy of a copper magnetic subsystem is realized by itself in $Cu_3Y(SeO_3)O_2Cl$ and $Cu_3Bi(SeO_3)O_2Br$. In these compounds, just one phase transition takes place, namely, the transition into the antiferromagnetic state. We assume that the same antiferromagnetic structure is realized in the title compound in the range $T_C < T < T_N$. Comprehensive studies of magnetic structures of these compounds performed by neutron scattering experiments [5,7] have shown that each copper plane possesses canted ferromagnetic order, while when neighboring planes are antiferromagnetically coupled, the effective magnetic field B_{eff}, acting on the RE ion by copper magnetic subsystem, is directed along the z axis. The splitting of Kramers doublet can arise under condition if its anisotropic g factor has a nonzero z component. Indeed, the splitting of each Kramers doublet in the mean-field approximation is governed by the formula $\Delta_k = \sqrt{\Sigma}(g_{ki} B_{\text{eff},i})^2$, where g_{ki}, $B_{\text{eff},i}$ are ith ($i = x,y,z$) components of the g factor and effective magnetic field acting on kth Kramers doublet, respectively. Such a relation enables the use of RE ions as a probe to get information on magnetic structures. Anisotropy of the g factor arises due to crystal-field effects and is related to the symmetry and bonding of the RE ion and its nearest environment. The absence of the splitting of the ground Kramers doublet of Sm^{3+}

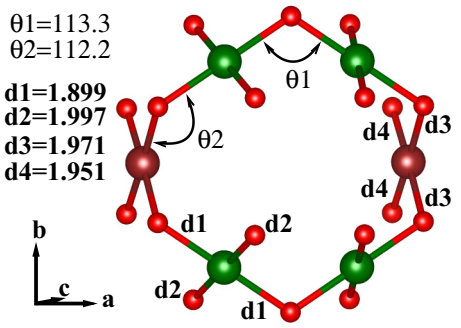

FIG. 11. The various Cu-O distances (in angstrom) and angles (in degree) within a $Cu1O_4$ and $Cu2O_4$ distorted squares in $Cu_3Sm(SeO_3)_2O_2Cl$.

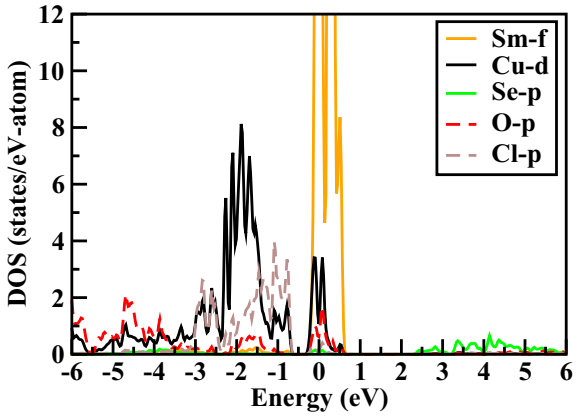

FIG. 12. Electronic density of states (DOS) calculated using density functional theory based tight binding (TB) LMTO in $Cu_3Sm(SeO_3)_2O_2Cl$. Energy axis is plotted with respect to Fermi energy.

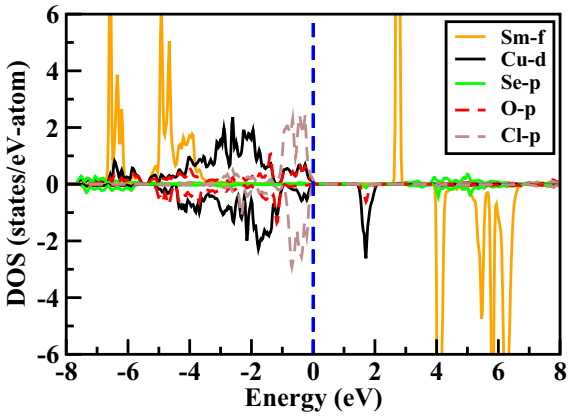

FIG. 14. The spin polarized density of states. The up channel of Cu-*d* is completely filled, while the down channel of Cu-*d* is partially filled.

in the temperature range $T_C < T < T_N$ can be explained, obviously, by the fact that $g_{0z}(Sm^{3+})$ is close to zero (here, symbol zero in g_{0z} relates to the ground Kramers doublet), while the excited Kramers doublet for the transition corresponding to the line L2 has, obviously, nonzero g_z. The splitting of the ground Kramers doublet arising at a temperature lower than T_C can be explained, definitely, by the rotation of B_{eff}, caused by spin-reorientation phase transition in the copper magnetic subsystem. The origin of this transition is the increasing magnetic anisotropy of RE ion. In an energy scale, the last one is equal to the half of Δ_0 per RE ion, and it increases with B_{eff} as far as the temperature is decreasing. When it became larger than the anisotropy of copper subsystem, the system tends to get the state with the minimal energy and experiences the spin-reorientation transition.

Spontaneous spin-reorientation transitions are generally classified in two main classes, namely first-order and second-order ones. The first one is characterized by a hopping change of the direction of magnetic moments and, hence, the abrupt change of the direction of B_{eff}, which leads, in its turn, to the abrupt change of the value of Δ_0. A smooth change of Δ_0 in the temperature interval from ~10 to 7 K allows us to classify the spin-reorientation phase transition in $Cu_3Sm(SeO_3)O_2Cl$ as a second-order one, during which the magnetic moments of the copper subsystem change their direction from one to another in the temperature interval mentioned above. The splitting of ground Kramers doublet Δ_0 follows the stepless change of B_{eff}.

Experimental data on $\Delta_0(T)$ were used to evaluate the contribution of samarium into thermodynamic properties, according to following equations [20]:

$$\chi_{\text{Sm}}(T) = \frac{1}{3} N_A \frac{M_{\text{Sm}}(0)^2}{k_B T} \left(\frac{1}{\cosh^2 \frac{\Delta_0(T)}{2k_B T}} \right), \quad (3)$$

$$C_{\text{Sm}}(T) = R \left(\frac{\Delta_0(T)}{k_B T} \right)^2 \frac{\exp(\Delta_0(T)/k_B T)}{(1+\exp(\Delta_0(T)/k_B T))^2}, \quad (4)$$

here $M_{\text{Sm}}(0)$ is the magnetic moment of samarium at the lowest temperature and the factor $1/3$ accounts for an averaging of randomly oriented crystallites in a polycrystalline sample. The dependences calculated with the aid of Eqs. 3 and 4 are shown in Figs. 10(b) and 10(c), respectively, and compared with the experimentally obtained data. The contributions to magnetic susceptibility $\chi_{\text{Sm}}(T)$ and specific heat $C_{\text{Sm}}(T)$ are masked by strong anomalies due to spin-reorientation transitions.

VI. FIRST PRINCIPLES CALCULATIONS

Electronic structure calculation within the framework of density functional theory (DFT) has been carried out for $Cu_3Sm(SeO_3)_2O_2Cl$ with an aim to figure out the underlying spin model. For the DFT calculations, we have used two different basis sets: (a) the muffin-tin orbital (MTO)-based

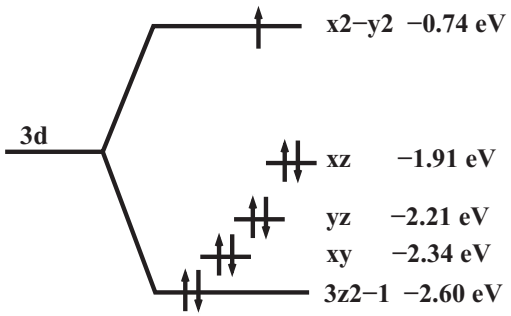

FIG. 13. Crystal field splitting of Cu-*d* orbital in the distorted square environment.

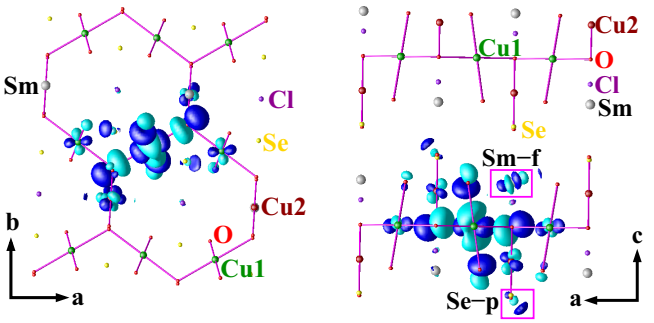

FIG. 15. The Wannier orbitals in the *ab* and *ac* plane.

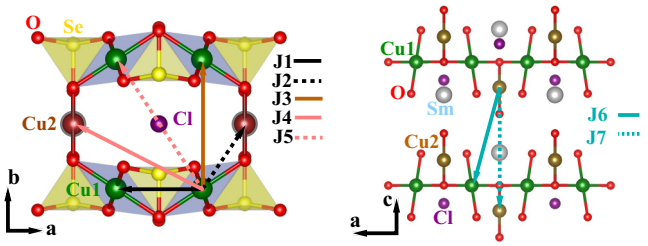

FIG. 16. The exchange paths for various magnetic interactions.

linear MTO (LMTO) method [21] and the Nth-order MTO (NMTO) method, namely, the NMTO method as implemented in the STUTTGART code [22] and (b) the plane-wave-based basis as implemented in the Vienna *ab initio* simulation package (VASP) [23]. For LMTO self-consistent electronic structure calculation, the basis set consisted of Cu spd, Sm sf, Se sp, O sp, and Cl sp. Nine different classes of empty spheres were used to space fill the system. The self-consistency was achieved by using 32 k-points in the irreducible Brillouin zone. The NMTO method, which relies on the self-consistent potential generated by the LMTO method, has been used for deriving the low-energy Hamiltonian defined in the basis of effective Cu-d Wannier functions by integrating out the degrees of freedom related to Sm, Se, O, and Cl. The real space representation of the low-energy Hamiltonian provides the information of crystal field splitting at inequivalent Cu sites as well as effective hopping interactions between two Cu sites. The energetically accurate plane-wave basis set calculations have been employed to calculate the total energy of different spin configurations to derive the magnetic exchanges from the total-energy method. For the self-consistent field calculations in the plane-wave basis, energy cutoff of 450 eV, and $4 \times 2 \times 6$ Monkhorst-Pack k-points mesh were found to provide a good convergence of the total energy ($\Delta E = 10^{-5}$ eV). The consistency between the calculations in the MTO and plane wave basis sets has been checked in terms of band structure, density of states, and magnetic moments, etc. The exchange correlation functional for the self-consistent calculations was chosen to be that of generalized gradient approximation (GGA) implemented following the Perdew-Burke-Ernzerhof prescription [24]. In the total energy calculations, the missing correlation energy at Cu and Sm sites beyond GGA calculations with supplemented Hubbard U (GGA + U) [25] were carried out, with a choice of $U = 8$ eV and $J_H = 1$ eV for both atoms. We considered a $2 \times 1 \times 2$ supercell and a $4 \times 6 \times 2$ Monkhorst-Pack k-point mesh for the total-energy calculations of various different spin configurations.

The Cu-O bond lengths of distorted squares and the various angles are shown in Fig. 11. A non-spin-polarized self-consistent calculation has been carried out for the title compound; the electronic density of states is presented in Fig. 12. The square environment of oxygen atoms surrounding Cu results in the Cu-d_{x2-y2} state at Fermi level pronouncedly mixed with O-p states. With Cu being in a 2+ oxidation state, all d states are completely filled except the d_{x2-y2} state, which is half filled. Therefore, the Cu-d_{x2-y2} state at Fermi level is primarily responsible for the electronic and magnetic behavior of the compound. We find that the distorted square crystal field splits the Cu-d levels according to that shown in the inset of Fig. 13. The corresponding spin-polarized density of states, obtained in a self-consistent spin-polarized DFT calculation, projected onto Cu-d, O-p, Cl-p, Se-p, and Sm-f states, is shown in Fig. 14. All of the d states are completely filled in the majority and minority spin channels except the minority channel of Cu-d_{x2-y2}, suggesting the nominal Cu^{+2} or d^9 valence of Cu. The O-p and Cl-p states are found to be mostly occupied, suggesting the nominal O^{-2} valence states and Cl^{-1} valence states, respectively. The oxidation state of Se and Sm atoms are +4 and +3, respectively. The O-p state shows finite, nonzero hybridization with the Cu-d state close to Fermi energy, which contributes to the super-exchange path of magnetic interaction between two Cu sites.

As mentioned above, in order to estimate the various Cu-Cu magnetic exchange interactions present in the compound, the NMTO-based downfolding technique was applied to construct Cu-d_{x2-y2}-only Wannier functions by downfolding all the degrees of freedom associated with O, Cl, Se, Sm, and the Cu

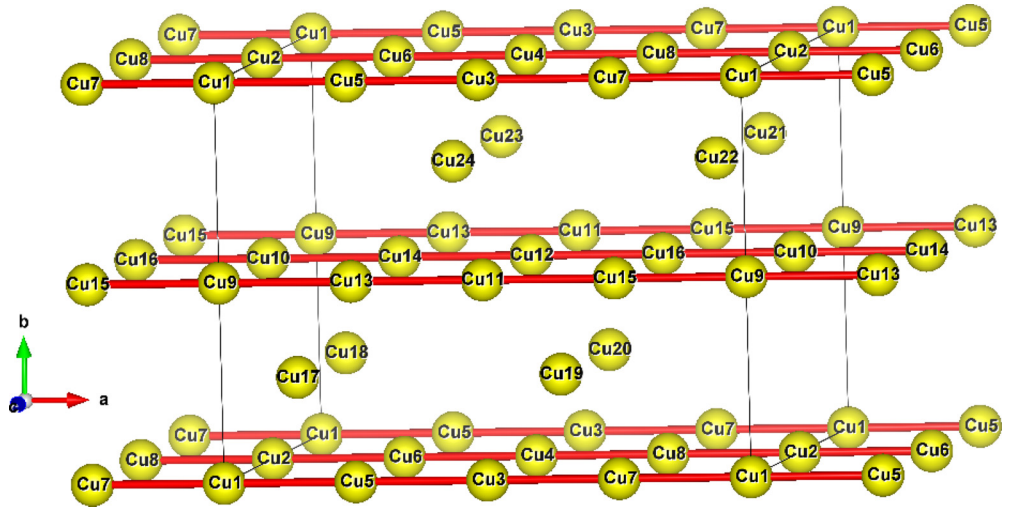

FIG. 17. The labeling of Cu sites in the $2 \times 1 \times 2$ supercell used for total energy calculations. The only nearest neighbor Cu atoms have been connected.

TABLE IV. Exchange interaction parameters in various francisites: comparative study of the results.

Interaction	Bond, meV	$Cu_3Sm(SeO_3)_2O_2Cl$	$Cu_3Y(SeO_3)_2O_2Cl$ [7]	$Cu_3Bi(SeO_3)_2O_2Cl$ [9]
Interlayer	J_1	−14.7	−11.7	−6.5
	J_2	−12.5	−7.3	−5.7
	J_3	3.2	3.6	4.7
	J_4	0.16	–	0.17
	J_5	−0.18	–	−0.26
Intralayer	J_6	0.44	0.69	−0.03
	J_7	0.09	−0.08	0.17

and keeping active only the Cu-d_{x2-y2} degrees of freedoms. This procedure provides renormalization of Cu-d_{x2-y2} orbitals due to hybridization from O-p, Cl-p, Se-p, Sm-f, and the other Cu-d orbitals. The effective Cu-d_{x2-y2}–Cu-d_{x2-y2} hopping interactions were obtained from the real space representation of the Hamiltonian in the effective Cu-d_{x2-y2} Wannier function basis. The effective Cu d_{x2-y2} Wannier function is plotted in Fig. 15. While the central part of these effective Wannier functions are shaped according to d_{x2-y2} symmetry, the tail sitting at the neighboring oxygen sites are shaped according to O-p_x/p_y symmetries, indicating strong pd_σ bonding between Cu and O. Finite contribution of Wannier orbitals on Se and Sm atoms indicates that the interlayer interactions are mainly mediated by the Se and Sm atoms.

The paths for the corresponding dominant magnetic interactions are shown in Fig. 16. We see that the magnetic interaction J_1 corresponding to hopping t_1 is mediated by Cu1 d-O p-Cu1 d superexchange paths where the Cu1-O-Cu1 bond angle is 113.3°, while J_2, corresponding to hopping t_2, is mediated by Cu1 d-O p-Cu2 d superexchange paths where the Cu1-O-Cu2 bond angle is 112.2°. J_3 corresponding to t_3 is mediated by the Cu1 d-O p-Cu2 d-O p-Cu1 d superexchange path, J_4 corresponding to t_4 is mediated by the Cu1 d-O p-Cu1 d-O p-Cu2 d superexchange path, and J_5 corresponding to t_5 is mediated by the Cu1 d-O p-Cu1 d-O p-Cu2 d-O p-Cu1 d superexchange path. The interlayer interactions J_6 and J_7, corresponding to t_6 and t_7, are the interactions between the Cu1&Cu2 and Cu2&Cu2 atoms, respectively. The magnetic interactions can be obtained from the knowledge of hopping interactions with a choice of Hubbard parameter U by using superexchange formula $4t^2/U_{\text{eff}}$. This, however, provides information of only the antiferromagnetic contributions. To account for that, we performed a total energy calculation of different spin configurations and extracted the magnetic exchanges by mapping the DFT energies to that of the Heisenberg model. For this purpose, as mentioned, we constructed a supercell of dimension $2 \times 1 \times 2$, giving rise to 24 Cu atoms in the unit cell, which are labeled in Fig. 17. The solutions of the calculated GGA + U energies of different spin configurations (refer to Table IV for the considered configurations and the energies) to the above defined Heisenberg model gave the estimate of Js. The dominant intralayer and interlayer magnetic exchange interactions J_{ij} with a choice of $U = 8\,\text{eV}$ and $J_{\text{H}} = 1\,\text{eV}$ are shown in Table V. The positive (negative) signs of interactions indicate the antiferromagnetic (ferromagnetic) nature of exchange interactions. Table IV also shows the corresponding exchange interactions for Bi and Y compounds, as reported in the literature. We find that the scale of exchange interaction parameters in $Cu_3Sm(SeO_3)_2O_2Cl$ estimated in first principles calculations is two times higher than that in $Cu_3Bi(SeO_3)_2O_2Cl$ and comparable with that in $Cu_3Y(SeO_3)_2O_2Cl$, which is reflected in the significantly enhanced temperature of long-range magnetic ordering.

Finally, we have checked the influence of strong spin-orbit coupling at the Sm site, on the Cu-Cu magnetic exchanges, by turning on the spin-orbit coupling at the Sm site. This resulted in an orbital moment of $-2.87\,\mu_B$ at the Sm site with a spin moment of $4.98\,\mu_B$. We note that the fully unquenched orbital moment for Sm^{3+} should be $-5\,\mu_B$, as expected from Hund's second rule. However, if the crystal field is sufficiently strong to prevent total unquenching, the orbital moment may be reduced to values like $-2.8\,\mu_B$, as obtained also for $SmCo_5$ [26]. We, however, found that the effect of spin-orbit coupling has little effect on the Cu-Cu magnetic exchanges, though certainly important for determining the magnetic structure, and magnetic phase transitions, as observed experimentally.

VII. CONCLUSION

The appearance of RE ions in position of bismuth ions in pristine mineral introduces the effects of interaction of the RE and transition metal subsystems. The synthesis of

TABLE V. Magnetic configurations of the Cu ions in the supercell for the states used to determine the magnetic interactions. The numbering of the Cu sites are as shown in Fig. 17. The last column gives the relative GGA + U energies in meV.

Cu→ Config.↓	1	2	3	4	5	6	7	8	9	10	11	12	13	14	15	16	17	18	19	20	21	22	23	24	ΔE (meV)
FM	+	+	+	+	+	+	+	+	+	+	+	+	+	+	+	+	+	+	+	+	+	+	+	+	0
AFM1	+	−	+	−	+	−	+	−	+	−	+	−	+	−	+	−	+	−	+	−	+	−	+	−	−8.194
AFM2	+	+	+	+	+	+	+	+	+	+	+	+	+	+	+	+	+	+	+	+	+	+	+	−	23.989
AFM3	+	+	+	+	+	+	+	+	+	+	+	+	+	+	+	+	+	+	+	+	+	+	−	−	48.163
AFM4	+	+	+	+	+	+	−	+	+	+	+	+	+	+	+	+	+	+	+	+	+	+	+	+	23.739
AFM5	−	+	+	+	+	+	−	+	+	+	+	+	+	+	+	+	+	+	+	+	+	+	+	+	32.774
AFM6	−	+	+	+	+	+	+	+	+	+	+	+	+	+	+	+	+	+	−	+	+	+	+	+	48.417
AFM7	+	+	+	+	+	+	−	+	+	+	+	+	+	+	+	+	+	+	−	+	+	+	+	+	35.228
AFM8	+	+	+	+	+	+	−	+	+	+	+	+	+	+	−	+	+	+	+	+	+	+	+	+	53.878

$Cu_3Er(SeO_3)_3O_2Cl$ [27], as well as several other RE francisites [10], was reported, but no information on physical properties are available. In $Cu_3Sm(SeO_3)_2O_2Cl$, the interplay of copper and samarium results in spin-reorientation transition. This is seen in pronounced anomalies of thermodynamic properties and is reflected in the splitting of ground Kramers doublet of Sm ions in addition to splitting of excited Kramers doublets below Néel temperature. The overall antiferromagnetic structure in $Cu_3Sm(SeO_3)_2O_2Cl$ is rather fragile being subject to metamagnetic phase transition prior to full saturation in moderate magnetic field. The similar response to the external magnetic field exhibited in thermodynamic measurements of $Cu_3Sm(SeO_3)_2O_2Cl$, as compared to $Cu_3Bi(SeO_3)_2O_2Br$ [5] and $Cu_3Y(SeO_3)_2O_2Cl$ [7], allows us to conclude that the canted magnetic structure is a general feature of the entire francisite family. The scale of exchange interaction parameters in $Cu_3Sm(SeO_3)_2O_2Cl$ estimated in first principles calculations is two times higher than that in $Cu_3Bi(SeO_3)_2O_2Cl$ and comparable with that in $Cu_3Y(SeO_3)_2O_2Cl$, which is reflected in the significantly enhanced temperature of long-range magnetic ordering.

ACKNOWLEDGMENTS

This paper was supported in part from the Ministry of Education and Science of the Russian Federation in the framework of Increase Competitiveness Program of National University of Science and Technology «MISiS» (No. K2-2015-075 and No. K4-2015-020) and by Act 211 of the Government of Russian Federation, Agreement No. 02.A03.21.0006. We acknowledge support from the Russian Foundation for Basic Research Grants No. 14-02-00111, No. 14-02-00245, No. 14-02-92693, No. 16-02-00021, and No. 16-03-00463. A.A. thankfully acknowledges UGC for providing his fellowship.

[1] A. Pring, B. M. Gatehouse, and W. D. Birch, Amer. Mineral. **75**, 1421 (1990).
[2] E. V. Nazarchuk, S. V. Krivovichev, O. Y. Pankratova, and S. K. Filatov, Phys. Chem. Miner. **27**, 440 (2000).
[3] P. Millet, B. Bastide, V. Pashchenko, S. Gnatchenko, V. Gapon, Y. Ksari, and A. Stepanov, J. Mater. Chem. **11**, 1152 (2001).
[4] K. H. Miller, P. W. Stephens, C. Martin, E. Constable, R. A. Lewis, H. Berger, G. L. Carr, and D. B. Tanner, Phys. Rev. B **86**, 174104 (2012).
[5] M. Pregelj, O. Zaharko, A. Günther, A. Loidl, V. Tsurkan, and S. Guerrero, Phys. Rev. B **86**, 144409 (2012).
[6] R. Becker and M. Johnsson, Solid State Sci. **7**, 375 (2005).
[7] K. V. Zakharov, E. A. Zvereva, P. S. Berdonosov, E. S. Kuznetsova, V. A. Dolgikh, L. Clark, C. Black, P. Lightfoot, W. Kockelmann, Z. V. Pchelkina, S. V. Streltsov, O. S. Volkova, and A. N. Vasiliev, Phys. Rev. B **90**, 214417 (2014).
[8] A. P. Ramirez, Ann. Rev. Mater. Sci. **24**, 453 (1994).
[9] I. Rousochatzakis, J. Richter, R. Zinke, and A. A. Tsirlin, Phys. Rev. B **91**, 024416 (2015).
[10] P. S. Berdonosov and V. A. Dolgikh, Russ. J. Inorg. Chem. **53**, 1353 (2008).
[11] V. Petricek, M. Dusek, and L. Palatinus, Z. Kristallogr. **229**, 345 (2014).
[12] S. R. J. Oliver, Chem. Soc. Rev. **38**, 1868 (2009).
[13] G. A. Bain and J. F. Berry, J. Chem Educ. **85**, 532 (2008).
[14] M. G. Banks, R. K. Kremer, C. Hoch, A. Simon, B. Ouladdiaf, J.-M. Broto, H. Rakoto, C. Lee, and M.-H. Whangbo, Phys. Rev. B **80**, 024404 (2009).
[15] C. Meyer, B. J. Ruck, J. Zhong, S. Granville, A. R. H. Preston, G. V. M. Williams, and H. J. Trodahl, Phys. Rev. B **78**, 174406 (2008).
[16] R. Nath, K. M. Ranjith, J. Sichelschmidt, M. Baenitz, Y. Skourski, F. Alet, I. Rousochatzakis, and A. A. Tsirlin, Phys. Rev. B **89**, 014407 (2014).
[17] J. P. Joshi and S. V. Bhat, J. Magn. Res. **168**, 284 (2004).
[18] Z. Wang, M. Schmidt, Y. Goncharov, V. Tsurkan, H.-A. Krug von Nidda, A. Loidl, and J. Deisenhofer, Phys. Rev. B **86**, 174411 (2012).
[19] M. N. Popova, S. A. Klimin, E. P. Chukalina, B. Z. Malkin, R. Z. Levitin, B. V. Mill, and E. Antic-Fidancev, Phys. Rev. B **68**, 155103 (2003).
[20] E. A. Popova, S. A. Klimin, M. N. Popova, R. Klingeler, N. Tristan, B. Büchner, and A. N. Vasiliev, J. Magn. Magn. Materials **331**, 133 (2013).
[21] O. K. Andersen and O. Jepsen, Phys. Rev. B **12**, 3060 (1975); Phys. Rev. Lett. **53**, 2571 (1984).
[22] O. K. Andersen and T. Saha-Dasgupta, Phys. Rev. B **62**, R16219 (2000).
[23] G. Kresse and J. Furthmüller, Phys. Rev. B **54**, 11169 (1996).
[24] J. P. Perdew, K. Burke, and M. Ernzerhof, Phys. Rev. Lett. **77**, 3865 (1996).
[25] V. I. Anisimov, I. V. Solovyev, and M. A. Korotin, Phys. Rev. B **48**, 16929 (1999).
[26] P. Larson, I. I. Mazin, and D. A. Papaconstantopoulos, Phys. Rev. B **67**, 214405 (2003).
[27] R. Berrigan and G. M. Gatehouse, Acta Cryst. C **52**, 496 (1996).